AGU PUBLICATIONS

JGR

Journal of Geophysical Research: Space Physics

RESEARCH ARTICLE

10.1002/2014JA020420

Key Points:
- A new 3-D MHD model for Saturn's magnetosphere is proposed
- The interaction between the solar wind and Saturn's magnetosphere

Correspondence to:
X. Feng,
fengx@spaceweather.ac.cn

Citation:
Wang, J., X. Feng, A. Du, and Y. Ge (2014), Modeling the interaction between the solar wind and Saturn's magnetosphere by the AMR-CESE-MHD method, *J. Geophys. Res. Space Physics*, *119*, 9919–9930, doi:10.1002/2014JA020420.

Received 23 JUL 2014
Accepted 25 NOV 2014
Accepted article online 2 DEC 2014
Published online 17 DEC 2014

Modeling the interaction between the solar wind and Saturn's magnetosphere by the AMR-CESE-MHD method

Juan Wang[1,2], Xueshang Feng[1], Aimin Du[3], and Yasong Ge[3]

[1]SIGMA Weather Group, State Key Laboratory for Space Weather, Center for Space Science and Applied Research, Chinese Academy of Sciences, Beijing, China, [2]College of Earth Sciences, Graduate University of Chinese Academy of Sciences, Beijing, China, [3]Key Laboratory of Earth and Planetary Physics, Institute of Geology and Geophysics, Chinese Academy of Sciences, Beijing, China

Abstract In this paper, the space-time conservation element and solution element (CESE) method in general curvilinear coordinates is successfully applied to the three-dimensional magnetohydrodynamic (MHD) simulations of the interaction between the solar wind and Saturn's magnetosphere on a six-component grid system. As a new numerical model modified for the study of the interaction between the solar wind and Saturn's magnetosphere, we obtain the large-scale configurations of Saturn's magnetosphere under the steady solar wind with due southward interplanetary magnetic field (IMF) conditions. The numerical results clearly indicate that the global structure of Saturn's magnetosphere is strongly affected by the rotation of Saturn as well as by the solar wind. The subsolar standoff distances of the magnetopause and the bow shock in our model are consistent with those predicted by the data-based empirical models. Our MHD results also show that a plasmoid forms in the magnetotail under the effect of the fast planetary rotation. However, somewhat differently from the previous models, we find that there are two flow vortices generated on the duskside under due southward IMF at Saturn. On the duskside, the clockwise one closer to the planet is excited by the velocity shear between the rotational flows and the sunward flows, while the anticlockwise one is generated from the velocity shear between the tailward flows along the magnetopause and the sunward flows.

1. Introduction

Since Saturn was successfully visited by Pioneer 11 in 1979, and then by Voyager 1 in 1980 and Voyager 2 in 1981, some essential knowledge about the structures and dynamics of Saturn's magnetosphere has been known. After 2004, Cassini started its detection of Saturn by collecting information about Saturn's atmosphere, ionosphere, magnetosphere, rings, and moons. From then on, Saturn has attracted much more attention. Cassini's extensive measurements of Saturn are favorable for developing a more complete 3-D simulation model for studying the dynamics of the Saturnian system that can validate the theory of Saturn.

The interaction between the solar wind and Saturn's magnetosphere involves the processes of the transportation of mass, momentum, and energy across the magnetopause. These processes include the magnetic reconnection between the interplanetary magnetic field and the planetary intrinsic magnetic field [*Dungey*, 1961], the Kelvin Helmholtz (K-H) instability [*Walker et al.*, 2011; *Fukazawa et al.*, 2012], and the plasmoids [*Zieger et al.*, 2010; *Jia et al.*, 2012] flowing from the nightside of Saturn toward the magnetotail. However, the interaction between the solar wind and Saturn's magnetosphere is still not well understood despite numerous magnetopause crossings by those previous spacecraft. Thus, 3-D numerical simulation is still a necessity.

Hansen et al. [2000] first developed a 3-D MHD simulation model for the solar wind interaction with Saturn's magnetosphere. They represented the interaction between the solar wind and Saturn with fast rotation and a dipole-like intrinsic magnetic field with the dipole axis closely aligned with the spin axis. Meanwhile, they added a simplified model of the neutral torus produced by Titan in their model. They found that the interaction between Saturn's magnetosphere and the solar wind depends strongly on the configuration of the interplanetary magnetic field. Several subsequent global MHD simulations of Saturn's magnetosphere [*Hansen et al.*, 2005; *Fukazawa et al.*, 2007a, 2007b; *Zieger et al.*, 2010] were then carried out. *Hansen et al.* [2005] improved their previous model by using the semirelativistic form of the MHD equations with an

implicit time-stepping algorithm and much better grid resolution and modified description of the source terms by adding the inner source due to the icy satellites. They studied Saturn's magnetosphere during the period of Cassini's initial approach and entry into the magnetosphere and got a reasonable agreement between the simulations and the observations.

The solar wind has a significant influence on the global configurations of Saturn's magnetosphere. According to *Alexeev et al.* [2006], the size of Saturn's magnetosphere depends on the solar wind dynamic pressure, and magnetosphere expands when the solar wind with low dynamic pressure passes it. Using 3-D MHD simulations, *Fukazawa et al.* [2007a] investigated the influence of the IMF B_z on Saturn's magnetospheric convection to conclude that the subsolar bow shock and magnetopause positions are sensitive to the changes of the solar wind dynamic pressure but insensitive to the changes of IMF B_z. At the same time, the study of *Fukazawa et al.* [2007a] pointed out that vortices formed in all cases of IMF B_z. Furthermore, *Jia et al.* [2012] improved their model through switching from a Cartesian grid system to a high-resolution but nonuniform spherical grid, which could reproduce better structures of the large-scale currents responsible for the coupling of magnetosphere and ionosphere. They even took the coupling of magnetosphere and ionosphere into consideration and simulated the interaction of the solar wind-magnetosphere-ionosphere system self-consistently at Saturn. *Jia et al.* [2012] also found that the location of Saturn's magnetopause is strongly determined by the solar wind dynamic pressure but is quite insensitive to the IMF orientation.

On the dawn and dusk of Saturn's magnetosphere, large vortices appear which are excited by the velocity shear between the rotational flows and the tailward solar wind flows [*Ogi et al.*, 2005]. In order to study the dynamics of the magnetospheric vorticity in Saturn's magnetosphere for northward IMF, *Fukazawa et al.* [2007b] carried out a global MHD simulation to suggest that vortices form on the dayside magnetopause initially and then propagate tailward. The dawn vortex forms first and then the dusk vortices follow. They found that a single clockwise vortex forms around the dawn while double vortices form at dusk with the one close to Saturn being clockwise and the other being counterclockwise. It is believed that vortices form along Saturn's magnetopause when the generation condition of Kelvin-Helmholtz (K-H) wave is met. The K-H waves at Saturn are similar to those found in simulations at Earth, but the main difference is that the rotational flows are significant for the boundary instability at Saturn [*Walker et al.*, 2011]. *Fukazawa et al.* [2012] performed an MHD simulation with a higher grid resolution than that of *Fukazawa et al.* [2007a, 2007b] to explore the consequences of the vortices and reconnection for the generation of field-aligned currents and auroras in Saturn's ionosphere.

Plasma is continuously supplied from the plasma sources to Saturn's inner magnetosphere, and the fast planetary rotation provides the mechanisms to remove the plasma produced there through plasmoid release in the magnetotail. As pointed out by *Jia et al.* [2012], a transient magnetic loop structure called plasmoid is spawned by magnetic reconnection resulting from internal process at Saturn, i.e., the so-called Vasyliūnas cycle in which the fast planetary rotation combined with the mass loading of flux tubes associated with the internal plasma sources leads to reconnection on closed magnetic field lines in the magnetotail. *Zieger et al.* [2010] studied plasma release from Saturn's nightside through a single-fluid global MHD model. They found that the release of the plasma in the magnetotail is continuous at high solar wind dynamic pressure, while plasmoids are pitched off periodically at medium dynamic pressure, and at low dynamic pressure the release of plasmoids becomes quasiperiodic or chaotic. Dynamics of Saturn's magnetosphere are intimately related to mass transport processes, such as radial diffusion, flux tube interchange, magnetic reconnection, and plasmoid formation. Recently, *Thomsen* [2013] made an overall review with recent progress and new questions for these processes at Saturn.

Both internal and external processes appear to be important in Saturn's magnetosphere. Saturn's magnetosphere is strongly determined by the solar wind but is also strongly influenced by the planetary rotation, the plasma sources, and the magnetic pole. The solar wind at Saturn has great different characteristics compared with the solar wind at Earth. The density is much smaller, and the magnitude of the interplanetary magnetic field is much weaker at Saturn. The fast rotation and large radius of Saturn produce enough torque on the plasma of the inner magnetosphere to bring it to corotate with the planet. At Saturn, there are also several neutral gas sources, including Saturn's ionosphere, the rings, icy satellites, and Titan. The neutrals from these sources are ionized by various processes such as photoionization and charge exchange to provide plasma for the inner magnetosphere. Moreover, Saturn has a strong intrinsic magnetic

field while its magnetic pole is opposite to that of Earth. Due to all these effects, Saturn's magnetosphere is quite different from Earth's.

In this paper, we numerically study the interaction between the solar wind and Saturn's magnetosphere by a new model, which is based on the AMR-CESE-MHD method in general curvilinear coordinates on a six-component grid system [*Jiang et al.*, 2010; *Feng et al.*, 2010, 2012]. The paper is organized as follows. Section 2 introduces the model by including the equations required, the simplifications, the assumptions, the computational domain, the initial conditions, and the boundary conditions. Section 3 briefly describes the main points of the model implementation. Section 4 is devoted to describing the numerical results about the global structures of Saturn's magnetosphere. Finally, discussions and conclusions are made.

2. Model Equations

The MHD equations used in our model are written in the following form

$$\frac{\partial \mathbf{U}}{\partial t} + (\nabla \cdot \mathbf{F})^T = \mathbf{S}_t (\equiv \mathbf{S} - \mathbf{L} + \mathbf{S}_{\nabla \cdot \mathbf{B}}), \tag{1}$$

where

$$\mathbf{U} = \begin{bmatrix} \rho \\ \rho \mathbf{u} \\ \mathbf{B}_1 \\ e_1 \end{bmatrix}, \tag{2}$$

$$\mathbf{F} = \begin{bmatrix} \rho \mathbf{u} \\ \rho \mathbf{u}\mathbf{u} + \mathbf{I}(p + \frac{1}{2}\mathbf{B}_1{}^2 + \mathbf{B}_1 \cdot \mathbf{B}_d) - \mathbf{B}_1\mathbf{B}_1 - \mathbf{B}_1\mathbf{B}_d - \mathbf{B}_d\mathbf{B}_1 \\ \mathbf{u}\mathbf{B} - \mathbf{B}\mathbf{u} \\ \mathbf{u}(e_1 + p + \frac{1}{2}\mathbf{B}_1{}^2 + \mathbf{B}_1 \cdot \mathbf{B}_d) - (\mathbf{u} \cdot \mathbf{B}_1)\mathbf{B} \end{bmatrix}^T, \tag{3}$$

$$\mathbf{S} = \dot{\rho} \begin{bmatrix} 1 \\ \mathbf{u}_n + \eta\rho(\mathbf{u}_n - \mathbf{u}) \\ 0 \\ \frac{1}{2}[\mathbf{u}_n^2 + \eta\rho(\mathbf{u}_n^2 - \mathbf{u}^2)] - \frac{1}{\gamma - 1}\eta p \end{bmatrix}, \quad \mathbf{L} = L_e \begin{bmatrix} \rho \\ \rho \mathbf{u} \\ 0 \\ \frac{1}{2}\rho \mathbf{u}^2 + \frac{1}{\gamma - 1}p \end{bmatrix} \tag{4}$$

$$\mathbf{S}_{\nabla \cdot \mathbf{B}} = -\nabla \cdot \mathbf{B}_1 \begin{bmatrix} 0 \\ \mathbf{B} \\ \mathbf{u} \\ \mathbf{u} \cdot \mathbf{B}_1 \end{bmatrix} \tag{5}$$

Here the energy density e_1 is given by $e_1 = \frac{1}{2}\rho \mathbf{u}^2 + \frac{p}{\gamma - 1} + \frac{1}{2}\mathbf{B}_1{}^2$, and ρ, $\mathbf{u} = (u_x, u_y, u_z)$, p, $\mathbf{B} (\equiv \mathbf{B}_1 + \mathbf{B}_d)$ are the mass density, the plasma velocity, the thermal pressure, and the magnetic field. $\mathbf{B}$ is split into the time-dependent part $\mathbf{B}_1 = (B_{1x}, B_{1y}, B_{1z})$ and the time-independent dipole part $\mathbf{B}_d$ to be given below. $\mathbf{u}_n = (u_{nx}, u_{ny}, u_{nz})$ refers to the velocity of the neutral particles taken under the assumption that the neutral torus rotates rigidly with Titan, that is $\mathbf{u}_n = \mathbf{\Omega}_T \times \mathbf{r}$, where $\mathbf{\Omega}_T$ is the angular speed of Titan with $|\mathbf{\Omega}_T| = 4.56 \times 10^{-6} s^{-1}$, and $\mathbf{r}$ is the position vector for a point in the neutral torus. Here x is directed from Saturn to Sun and z is the direction of the rotation axis of Saturn (pointing to the north). The ratio of specific heats is γ (taken to be 5/3), and $\mathbf{I}$ is a unit tensor.

For the initial study of Saturn, we simplify the plasma sources of Saturn's magnetosphere by neglecting the sources and sinks associated with Saturn itself and the icy satellites but only consider the effects of Titan suggested by *Hansen et al.* [2000]. Thus, a simplified model of the neutral torus centered around Titan's orbit at about $20.2R_S$ ($R_S = 6.027 \times 10^7$ m is the radius of Saturn) is employed in our model. The neutrals from the torus are ionized by various processes such as photoionization, electron impact ionization, charge exchange, ion-neutral friction, and ion-electron recombination. These processes lead to a significant source of plasma for Saturn's inner magnetosphere. The source vector, $\mathbf{S}$, describes the mass loading by freshly ionized particles and ion-neutral friction. The loss vector, $\mathbf{L}$, describes the process of recombination between ions

and electrons. In addition, $\dot{\rho}$, η, and L_e stand for the mass addition rate, the ion-neutral friction coefficient, and the loss coefficient, respectively. Here the expressions of $\dot{\rho}$, η, L_e, **S**, and **L** are taken as the same as described by *Hansen et al.* [2000].

To improve the accuracy of the calculations of the planet having strong intrinsic magnetic field such as Saturn, the scheme solves for only the deviation of the magnetic field from the intrinsic magnetic field, namely, $\mathbf{B}_1 = \mathbf{B} - \mathbf{B}_d$ [*Tanaka*, 1994], where $\mathbf{B}_d$ is the intrinsic magnetic field of Saturn corresponding to a dipole magnetic field with a strength of 2.08×10^{-5}T at the equatorial surface of Saturn. For reducing the complexity of our model, we assume that the dipole axis is aligned with the spin axis. For dealing with the divergence of the magnetic field, the Powell's source terms $\mathbf{S}_{\nabla\cdot\mathbf{B}}$ [*Powell et al.*, 1999] shown by equation (5) have been added in the MHD equations.

The primitive variables **r**, ρ, **u**, t, **B**, and p in equation (1) have been normalized by their corresponding characteristic values R_S, ρ_0, $B_0/\sqrt{\mu_0\rho_0}$, $R_S\sqrt{\mu_0\rho_0}/B_0$, B_0, and B_0^2/μ_0. Here μ_0 is the permeability of vacuum, $B_0 = 2.08 \times 10^{-5}$ T (the field strength at the equatorial surface of Saturn) and $\rho_0 = 1.67 \times 10^{-22}$ kg · m^{-3} (the solar wind density).

The computational domain used in this calculation extends from $3.0R_S$ to $226.5R_S$. Near the surface of Saturn, the magnetic field is very strong such that the Alfvén velocity is very large. In order to keep the computation time step from becoming too small, we set the inner boundary at $3.0R_S$. At the outer boundary, the fixed inflow boundary conditions are applied at the dayside, while the free-flow boundary conditions are used at the nightside. According to *Hansen et al.* [2000], at the inner boundary the density and the pressure are fixed, the velocities are fixed to coincide with the rotation of Saturn (implying a zero radial velocity), and the magnetic field is taken to be only the intrinsic planetary dipole field.

For the model validation, we use a simple and steady solar wind as the input: $\rho_{sw} = 0.1$ amu cm^{-3}, $u_{xsw} = -400$ km/s, $T_{sw} = 1.8 \times 10^5$ K, and $B_{zsw} = -0.5$ nT.

3. The CESE Method

The CESE method has been successfully used and shown its powerful capability in space weather modeling [*Feng et al.*, 2007, 2010, 2011, 2012; *Zhou and Feng*, 2013]. The CESE method treats space and time as a unity, which is the key difference between the CESE method and most existing numerical difference schemes. In the CESE method, both the variables and their first-order spatial derivatives are introduced as solving variables. It can capture shocks within a few grid points without using Riemann solvers, but with the introduced damping effect being controllable.

The AMR-CESE-MHD method in general curvilinear coordinates for solar wind modeling has been detailed by *Feng et al.* [2007, 2010, 2012] and *Jiang et al.* [2010]. In this code, the MHD equations are solved with the adaptive mesh refinement (AMR) technique in curvilinear coordinates based on coordinate transform. For the detailed description of AMR-CESE-MHD method, please refer to these papers. Here we just briefly state those points specified for studying the interaction between the solar wind and Saturn's magnetosphere.

3.1. The Six-Component Grid and Curvilinear Coordinates Transform

Saturn's geometry can be seen as being spherically shaped, and thus, it is natural to use the spherical grid cells to describe the computational domain of spherical shell. In this manner, the inner boundary conditions can be directly given on the boundary grid cells without any interpolation, although Cartesian grids can work well [*Ogi et al.*, 2005; *Fukazawa et al.*, 2007a, 2007b, 2012]. However, spherical polar grids raise numerical difficulties associated with the presence of both singularities and grid convergence near the poles and consequently may negatively impact the accuracy and the performance of the numerical procedure. To overcome these problems, *Feng et al.* [2010] introduced the six-component grid to characterize computational domain better than other grid systems but with fewer grid cells.

The six-component grid partitions the computational domain into six identical component meshes with partial overlapping regions (see Figure 1), with each component identically defined by a low-latitude spherical domain

$$\left(\frac{\pi}{4} - \delta \le \theta \le \frac{3\pi}{4} + \delta\right) \cap \left(\frac{3\pi}{4} - \delta \le \phi \le \frac{5\pi}{4} + \delta\right), \tag{6}$$

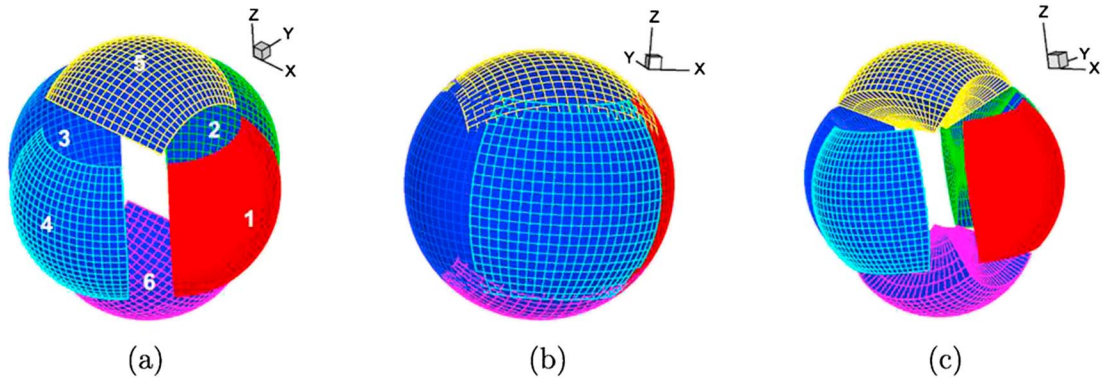

Figure 1. Six-component grid: (a) a spherical overset grid composed of six identical components; (b) dividing a sphere into six identical components with partial overlap; and (c) stacking the spherical meshes of each component up in the radial direction. Adopted from *Feng et al.* [2010].

where $\delta = 2\Delta\theta$ is proportionally dependent on the grid spacing which is entailed for the minimum overlapping regions between components. The six-component grids can be transformed into each other by coordinate transformation such that the basic equations, the numerical grid distribution, and all numerical tasks are identical on each component. These attributes are convenient to realize parallel computation. Hence, we only need to describe the grid partition and the associated coordinate transform without distinguishing them.

In both θ and ϕ directions, grid points are evenly distributed. The mesh numbers of the latitude and longitude are respectively denoted by N_θ and N_ϕ. So we get $N_\theta = N_\phi = 33$, $\Delta\theta = (\theta_{\max} - \theta_{\min})/(N_\theta - 1) = \pi/64$, and $\Delta\phi = (\phi_{\max} - \phi_{\min})/(N_\phi - 1) = \pi/64$, where $\theta_{\min} = \pi/4$, $\theta_{\max} = 3\pi/4$, $\phi_{\min} = 3\pi/4$, and $\phi_{\max} = 5\pi/4$. On each component in physical space, $\theta_j = \theta_{\min} + j\Delta\theta, j = 0, 1, 2, ..., (N_\theta - 1)$, and $\phi_k = \phi_{\min} + k\Delta\phi, k = 0, 1, 2, \cdots, (N_\phi - 1)$.

In the r direction, a new variable ξ is introduced as a reference coordinate, which is exponentially related with r by $r = a^\xi$, $a = 1.481$ [*Feng et al.*, 2012]. In order to make the cells more regular in the reference space, we need to choose $\Delta\xi = \log_a(1 + \Delta\theta)$ such that $\Delta r = r\Delta\theta$. Thus, the grid cell in the reference space (ξ, η, ζ) is a rectangular box. Meanwhile, the curvilinear coordinates (ξ, η, ζ) used in our CESE solver refer to (ξ, θ, ϕ) here. The inner boundary in our model is at $3.0R_S$ and the outer boundary is at about $226.5R_S$, such that each component in the physical grids is identically defined by $2.797 < \xi < 13.81$, $\pi/4 - \delta \le \eta \le 3\pi/4 + \delta$, and $3\pi/4 - \delta \le \zeta \le 5\pi/4 + \delta$ in the reference space, where $\Delta\theta = \Delta\phi = \Delta\eta = \Delta\zeta = \pi/64$.

3.2. The Governing MHD Equations in Curvilinear Coordinates

In this section, the CESE solver [*Feng et al.*, 2006, 2010] for the governing MHD equations in curvilinear coordinates is briefly described.

By using Gauss's divergence theorem on a space-time region V in four dimensions to equations (1), we have

$$\oint_{S(V)} \mathbf{q}_m \cdot d\mathbf{S} = \int_V S_{tm} dV, \quad m = 1, \cdots, 8. \tag{7}$$

Here $\mathbf{q}_m = (\mathbf{F}_m, U_m)$, $S(V)$ is the boundary of the region V, and $\mathbf{q}_m \cdot d\mathbf{S}$ is the space-time flux leaving the region of V through the surface element $d\mathbf{S}$.

By evaluating the space-time flux, equation (7) can be approximated by its discrete counterpart as

$$\oint_{S(CE)} \mathbf{q}_m \cdot d\mathbf{S} = \int_{CE} S_{tm} dV, \tag{8}$$

where CE is the conservation element of the solution point Q [*Feng et al.*, 2006].

Then we can get

$$(U_m)_Q^n - \frac{\Delta t}{2}(S_{tm})_Q^n = (U_{Hm})^{n-\frac{1}{2}}, \tag{9}$$

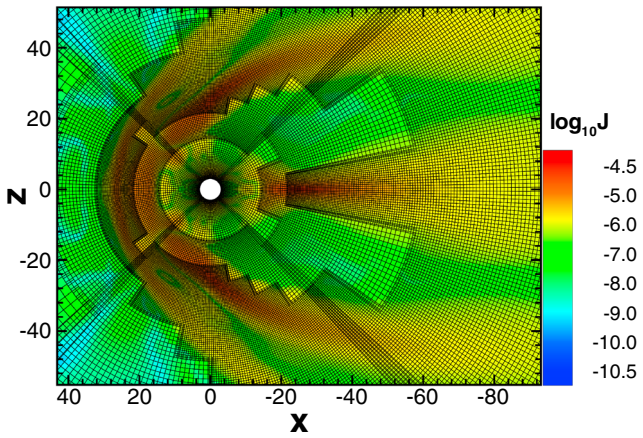

Figure 2. The grid cells in the *X-Z* plane corresponding to Figure 5 (left), where the black quadrilaterals denote the grid cells cut through the *X-Z* plane and the overset grids between components can be clearly seen near the lines of $\theta = \frac{\pi}{4}$ and $\frac{3\pi}{4}$.

which is similar to the counterpart given by *Feng et al.* [2006] and *Jiang et al.* [2010]. Here $\mathbf{U}_H$ is the local homogeneous solution (i.e., the solution for $\mathbf{S}_t = 0$ locally). For the concrete form of $\mathbf{U}_H$, we can refer to *Jiang et al.* [2010]. Thus, given the values of the variables $(\mathbf{U}, \mathbf{U}_x, \mathbf{U}_y, \mathbf{U}_z)$ at the $\left(n - \frac{1}{2}\right)$th time level, by solving the nonlinear equation (9) with Newtonian iteration method, we can get the values $(\mathbf{U}, \mathbf{U}_x, \mathbf{U}_y, \mathbf{U}_z)$ at nth time level with the corresponding derivatives $(\mathbf{U}_x, \mathbf{U}_y, \mathbf{U}_z)$ provided by *Feng et al.* [2006]. This briefly finishes the description of the CESE-MHD solver in the physical space (x, y, z).

In practice, our CESE-MHD solver is implemented in the reference space as follows. The MHD equations (1) can be written into conservation form from the physical space (x, y, z) to the reference space $(\xi, \eta, \zeta) = \left(\log_a\left(\sqrt{x^2+y^2+z^2}\right), \arccos\left(z/\sqrt{x^2+y^2+z^2}\right), \arctan(y/x)\right)$ as follows

$$\frac{\partial \hat{\mathbf{U}}}{\partial t} + (\hat{\nabla} \cdot \hat{\mathbf{F}})^T = \hat{\mathbf{S}}_t, \tag{10}$$

where $\hat{\mathbf{U}} = J\mathbf{U}$, $\hat{\nabla} = (\partial_\xi, \partial_\eta, \partial_\zeta)$, $\hat{\mathbf{F}} = J\mathbf{F} \cdot \nabla(\xi, \eta, \zeta)^T$, $\hat{\mathbf{S}}_t = J\mathbf{S}_t$, and $J = |\frac{\partial(x,y,z)}{\partial(\xi,\eta,\zeta)}|$ is the Jacobian determinant of the transformation. With these preparations, the CESE-MHD solver in curvilinear coordinates follows the same steps as those for the CESE-MHD solver in the physical space.

The CESE-MHD solver in curvilinear coordinates is established with adaptive mesh refinement implementation [*Feng et al.*, 2012, 2013]. In the simulation here, current system is a key structure. Thus, in order to capture the current sheet, the curl of the magnetic field is used as our refinement strategy

$$\chi = \sqrt{V}\frac{|\nabla \times \mathbf{B}|}{|\mathbf{B}| + \epsilon\sqrt{p}}. \tag{11}$$

Here $\mathbf{B}$ is the magnetic field, p is the thermal pressure, and V is the volume of the cell. The factor $\epsilon << 1.0$ is introduced into equation (11) to avoid the zeroness of denominators. The standard deviation about zero $\sigma = \sqrt{\sum_{i=1}^{N} \chi_i^2 / N}$ of χ is calculated, where N is the total number of all the cells in the computational domain. Multiplying σ by properly chosen factors gives the thresholds of refining or coarsening blocks. In this model, we choose to multiple σ by $2.0 \sim 3.0$ as the refining threshold and by $0.5 \sim 0.8$ as the coarsening threshold. By choosing different factors, we can achieve different degrees of mesh refinement.

After every computation time step, the code first checks whether the blocks need to be coarsened or refined by using the AMR criterion and then finishes the flux interpolation and guardcell filling for newborn cells. The six identical components envelope a spherical surface with partial overlapping areas, where the values can be determined by third-order Lagrange interpolation from the values in its neighbor components. For details one can refer to *Feng et al.* [2012, 2013].

4. Numerical Results

In this section, we present the simulation results of Saturn's global magnetospheric configurations and study the dynamics in the magnetosphere.

As explained above, the AMR is carried out based on the refining and coarsening thresholds, and three levels of grid refinements are used in this study. While the code is running, the grid resolution is altered dynamically. Initially, each component in the computational domain is divided into $11 \times 4 \times 4$ blocks

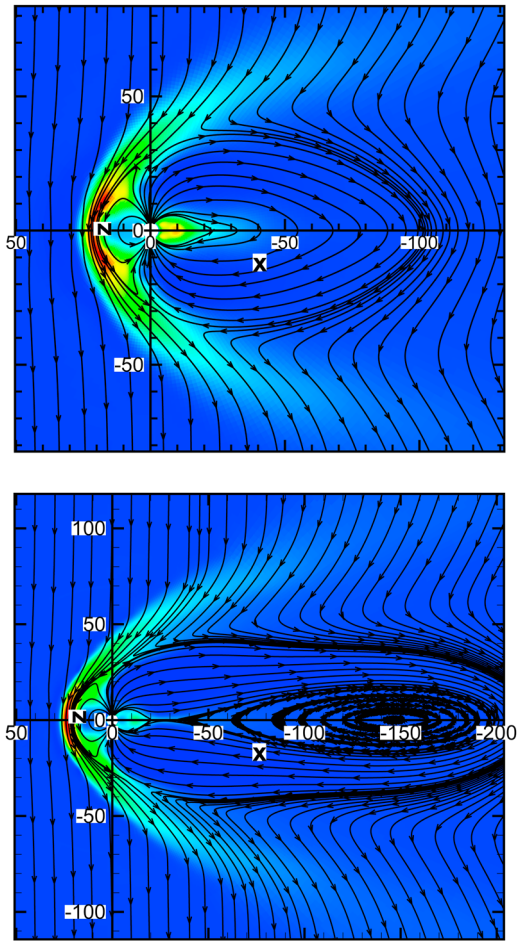

Figure 3. The global structure of Saturn's magnetosphere in the noon-midnight meridian plane under due southward IMF. The state of Saturn's magnetosphere (top) before and (bottom) after a plasmoid forms in the magnetotail. Black lines with arrows are magnetic field lines, and the color contour represents the thermal pressure.

(1056 blocks in total) with each block consisting of 8 × 8 × 8 grid cells. The AMR grid cells used during the calculation are displayed in Figure 2. Eventually, the computational domain is divided into about 17,058 blocks with each having 8 × 8 × 8 grid cells, yielding a total number of nearly 8.7 million cells, and the size of the cell in the computational domain varies from $0.15R_S$ to $2.83R_S$.

We map the magnetic field lines in the 2*D* plane. Figure 3 just shows the global large-scale structures of Saturn's magnetosphere in the noon-midnight meridian plane for due southward IMF. Black lines with arrows are the magnetic field lines, and the color contour represents the thermal pressure. Figure 3 shows the state of Saturn's magnetosphere before (top) and after (bottom) a plasmoid forms in the magnetotail. Figure 3 helps us understand the dynamics of the interaction between the solar wind and Saturn's magnetosphere under due southward IMF. We can see that when the solar wind passes Saturn, it severely compresses the dayside of the planet, and the bow shock forms before the magnetosphere. The Dungey cycle reconnection between the IMF and the planetary magnetic field takes place at the nightside of the cusp regions. After a prolonged period of running time, we obtain a nearly closed magnetosphere for Saturn which is open only over small regions occupied by the two cusps for due southward IMF. Since Saturn's magnetic dipole is opposite to that of Earth, Saturn's magnetospheric configuration under due southward IMF is somewhat similar to Earth's under due northward IMF.

In addition to the Dungey cycle reconnection in Saturn's magnetosphere, there is another process called the Vasyliūnas cycle reconnection. The Vasyliūnas cycle [*Vasyliūnas*, 1983] reconnection is also found in our simulation. Figure 3 (bottom) just shows a snapshot of the magnetotail plasmoid during its development. The plasmoid formation is dominantly caused by the fast planetary rotation. The fast planetary rotation leads to the centrifugal acceleration for the outward moving heavy plasma, and the plasma continues moving outward unless there is some process that can barrier it. The outward motion of the heavy plasma forces the magnetic field lines become so stretched and thin that magnetic reconnection begins to take place in the plasma sheet, and an "O"-like plasmoid is formed little by little and then grows up into a very large plasmoid gradually while moving down the magnetotail. Thus, the magnetotail stretches very far away from the planet. After a sufficient long period of time, under the effects of the outward moving plasma and the fast planetary rotation, the planetary field lines are stretched long enough that they become too weak to confine the plasmoid, and the plasmoid pinches off, and then the plasmoid leaves Saturn's magnetosphere freely. These newly closed magnetic field lines on the planetary side start to shrink because the magnetic stress drags the equatorial part of the field lines toward the planet, restoring the planetary plasma to corotate with the planet, which is the process of dipolarization. *Zieger et al.* [2010] have confirmed the plasma release phenomena in Saturn's magnetosphere by a series of 3-D MHD simulations. The plasmoid formation and release have been testified by both magnetic field data [*Jackman et al.*, 2009, 2011] and plasma data [*Hill et al.*, 2008]. In situ signatures of dipolarization of reconnected flux returning to the inner

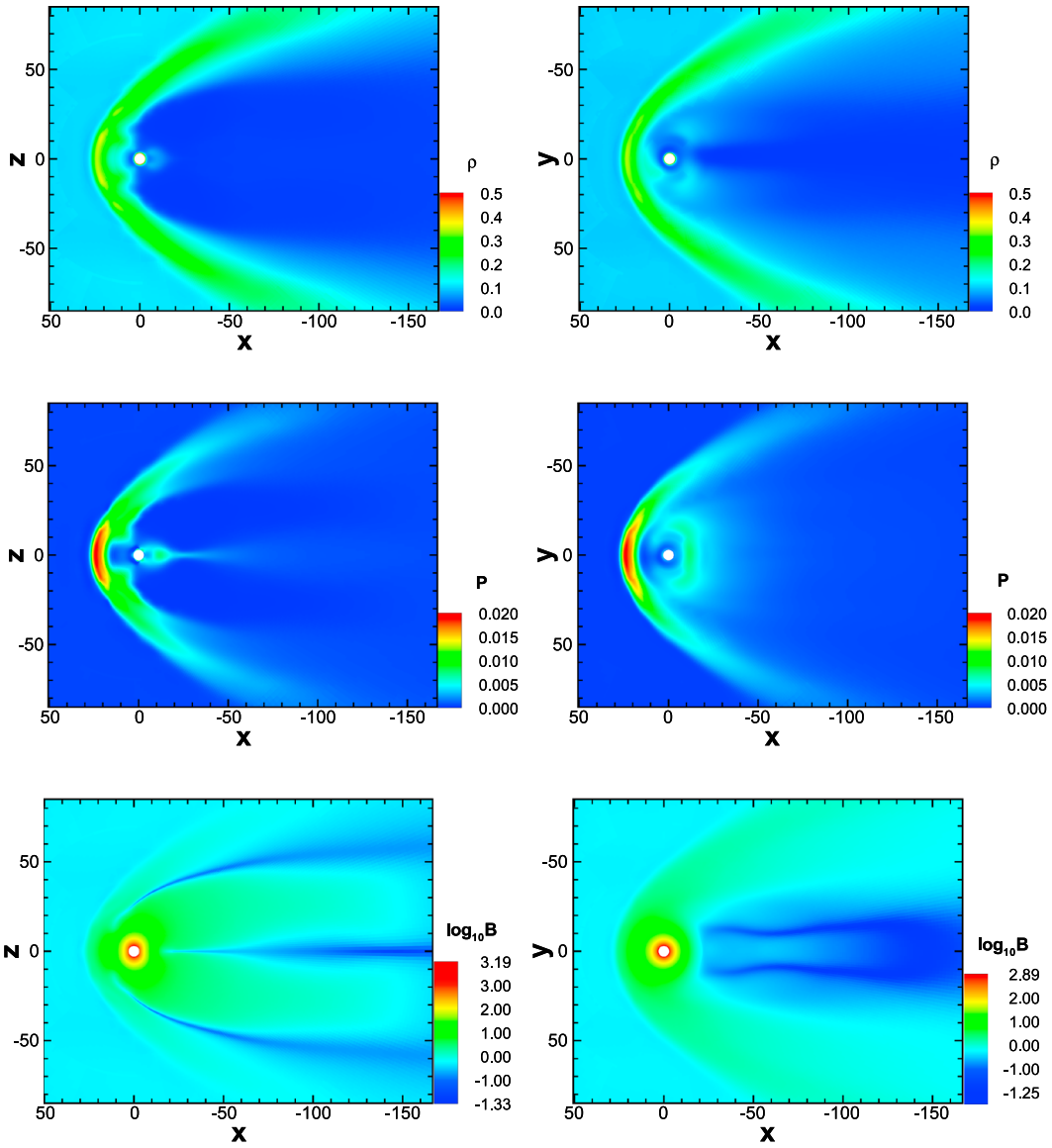

Figure 4. Contours of (top row) plasma density (unit: cm^{-3}), (middle row) thermal pressure (unit: nPa), and (bottom row) 10-based logarithm of the magnetic strength (unit: nT) in (left column) the meridian plane and (right column) the equatorial plane corresponding to Figure 3 (bottom).

magnetosphere have been presented by the magnetometer data [*Russell et al.*, 2008; *Jackman et al.*, 2013]. Moreover, the plasmoid formation and the dipolarizations are both identified by the remotely sensed energetic neutral atom (ENA) imagers brightenings [*Mitchell et al.*, 2005].

Figure 4 shows the contours of plasma density, thermal pressure, and 10-based logarithm of magnetic strength in the meridian plane and the equatorial plane. The current system is an important structure in such magnetosphere simulations. The field-aligned currents are responsible for the coupling of the magnetosphere and the ionosphere. We present the current density distribution in the noon-midnight meridian plane and the equatorial plane in Figure 5 which shows that the bow shock, the magnetopause, and the magnetotail current sheets are well captured by the adaptive mesh refinement. The magnetopause separates the shocked solar wind from the region dominated by the planetary magnetic field. It can be considered as a tangential discontinuity across which the total pressure can be balanced. According to *Jia et al.* [2012], Saturn's upstream magnetopause is primarily determined by the balance between the total pressures inside and outside the magnetosphere.

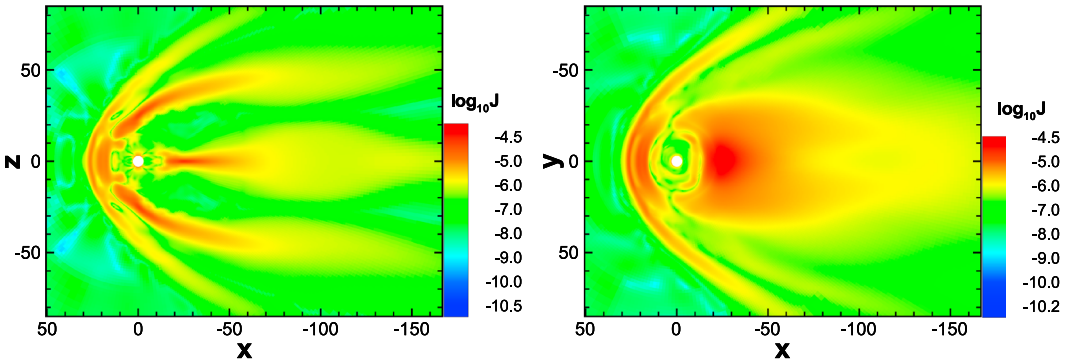

Figure 5. The 10-based logarithm of current density (unit: $\mu A/m^2$) distribution in (left) the meridian plane and (right) the equatorial plane corresponding to Figure 3 (bottom).

In what follows we compare the standoff distance of the magnetopause (MP) from our MHD simulation results with the empirical magnetopause model developed by *Kanani et al.* [2010]. The magnetopause standoff distance from the empirical model is calculated based on the formula $R_{MP} \sim 10P_{dyn}^{-1/(5\pm0.8)}$, where P_{dyn} (in unit nPa) is the dynamic pressure of the solar wind. From the parameters of the solar wind used in the MHD model, the magnetopause standoff distance is predicted to be $18.7R_S \sim 23.7R_S$ by the empirical model. We extract R_{MP} from the MHD results by locating the MP at the local maxima of the magnetopause current [*Palmroth et al.*, 2001; *Samsonov et al.*, 2007] as shown by Figure 6. The MHD results give that the location of subsolar MP is at about $20.7R_S$, which is in the estimated range of the empirical model. Thus, the subsolar magnetopause standoff distances extracted from our MHD model agree with that predicted by the empirical magnetopause model.

Figure 4 shows that the bow shock (BS) is formed when the solar wind encounters the magnetosphere. Hence, the incident solar wind conditions and the size and shape of the magnetosphere determine the size and shape of the bow shock. The standoff in the empirical bow shock model developed by *Farris and Russell* [1994] is given as

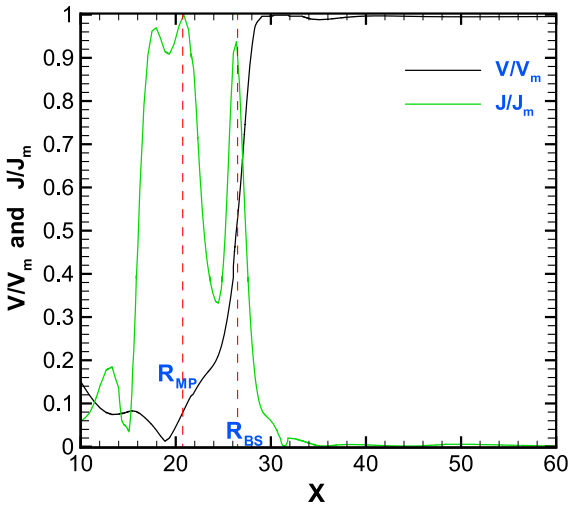

Figure 6. Profiles of V/V_m (black color) and J/J_m (green color) along x axis, where V and J stand for flow velocity and current density while V_m and J_m stand for the maxima of flow velocity and current density in the range of $10.0R_S \le x \le 60.0R_S$. The magnetopause is marked as the local maxima in the current density, and the bow shock location is confirmed by the velocity jump. The standoff distances of the magnetopause and the bow shock are indicated by R_{MP} and R_{BS}, respectively.

$$R_{BS} = R_{MP}\left[1 + 1.1\frac{(\gamma-1)M_{ms}^2 + 2}{(\gamma+1)(M_{ms}^2-1)}\right], \quad (12)$$

which depends on the upstream solar wind fast magnetosonic Mach number M_{ms}, the subsolar magnetopause standoff distance R_{MP}, and the ratio of specific heats γ (taken as 5/3 here). The subsolar bow shock standoff distance calculated from the empirical model is $26.9R_S$ with $R_{MP} = 20.7R_S$ given above. *Jia et al.* [2012] showed V_x in Figure 13 of their paper. We find that the thickness of the bow shock from our MHD results as shown by Figure 6 looks slightly larger than that inferred from the color contour of V_x in *Jia et al.* [2012]. However, we just focus on the location of the bow shock here. Following the method used by *Hansen et al.* [2005], we extract the subsolar bow shock by locating it at the midpoint of the MHD velocity jump along the x axis. Figure 6 shows that the MHD model gives $R_{BS} = 26.5R_S$ that almost coincides with that estimated from the empirical model.

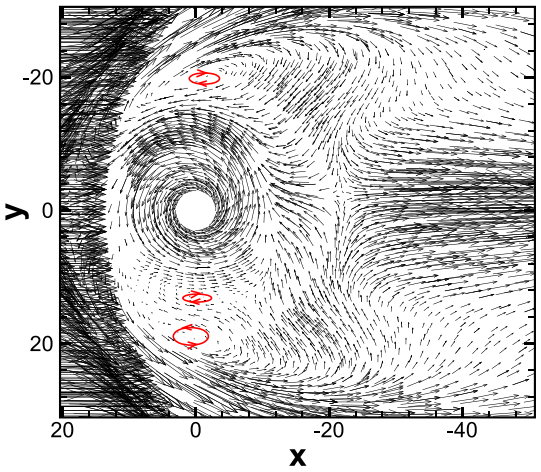

Figure 7. Flow vectors in the equatorial plane corresponding to Figure 3 (bottom).

Figure 7 shows the flow vectors (black arrows) in the equatorial plane. We can clearly see that the plasma in the inner magnetosphere corotates with Saturn under high torque produced by fast rotation and interacts with the incident solar wind. Besides, we also find that a clockwise vortex forms on the dawnside while two vortices (the one closer to Saturn is clockwise and the other is anticlockwise) form on the duskside. We infer that their possible formation mechanisms may be as follows. As a fast rotational planet, Saturn behaves like a rotating wheel driving the surrounding plasma to corotate with it. From Figure 7, we can clearly see that some of the tailward flows along the dawnside and the duskside magnetopause are reversed to be rotational (called the reversed flows below). On the dawnside, a clockwise vortex forms near the dawn magnetopause where the rotational flows are opposite to the tailward flows and the velocity shear takes place. On the duskside, some of the reversed flows shunt into the sunward direction (called the sunward flows below) and some turn to corotate with Saturn. These sunward flows are opposite to the rotational flows and the tailward flows along the magnetopause. Thus, on the duskside, a clockwise vortex closer to the planet forms that results from the velocity shear between the rotational flows and the sunward flows. Moreover, an anticlockwise vortex larger than the clockwise one on the duskside is excited by the velocity shear between the tailward flows along the magnetopause and the sunward flows. From the MHD simulation results, we deduce that the two vortices on the duskside appear before the plasmoid forms in the magnetotail. In Figure 8, we have plotted the profiles of $|V_x|$ from 10.0 R_S to 20.0 R_S along y axis ($x = 0$) that crosses the two vortices on the duskside before, during, and after the plasmoid formation. The red, purple, and green/blue solid lines indicate the $|V_x|$ profile before, during, and after plasmoid formation, respectively. Figure 8 shows that the two vortices on the duskside remain stable as time evolves. It may be inferred that the formation mechanism of the vortices on the dusk is independent on the plasmoid formation in the magnetotail.

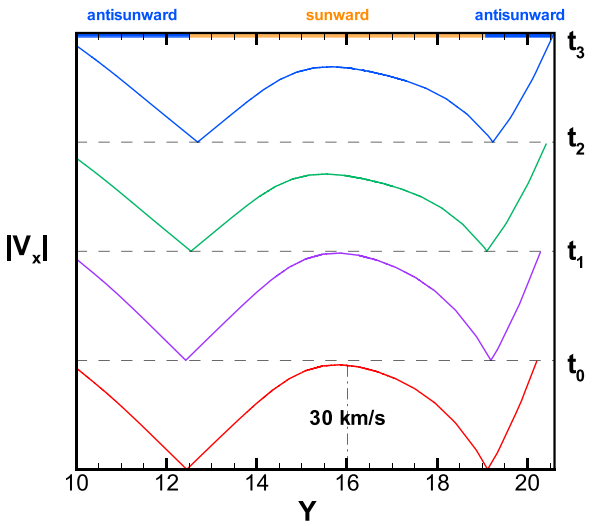

Figure 8. The profiles of $|V_x|$ from about 10.0R_S to 20.0R_S along y axis ($x = 0$) that crosses the two vortices on the duskside before, during, and after the plasmoid formation in the magnetotail. The red, purple, and green/blue solid lines indicate the $|V_x|$ profile before, during, and after plasmoid formation, respectively.

5. Conclusions

In this paper, we used the AMR-CESE-MHD method developed by *Feng et al.* [2012] to study the interaction of the solar wind with Saturn's magnetosphere. Under the steady solar wind with due southward interplanetary magnetic field (IMF) conditions, the numerical results of the configurations of Saturn's magnetosphere show a good consistency with those published by *Hansen et al.* [2000], by providing a good indication of the features such as the bow shock, the magnetopause, and the magnetotail current sheets. At the same time, the subsolar standoff distance of the magnetopause and the bow shock in our model are consistent with those predicted by the data-based empirical models [*Kanani et al.*, 2010; *Farris and*

Russell, 1994]. The MHD model reasonably shows that plasmoid forms in the magnetotail under the effect of the fast planetary rotation for due southward IMF. Moreover, we find that a clockwise vortex forms on the dawnside and two vortices form on the duskside with the one closer to the planet being clockwise and the other being anticlockwise. Their possible formation mechanisms are due to the velocity shear between the tailward flows, the rotational flows, and the sunward flows.

Several runs with different grid refinements show that low resolution can smear the delicate structure due to the numerical dissipation. Fine grid resolution (at least three levels of refinements in our case) significantly reduces the numerical dissipation. In such large-scale simulation, the use of AMR technique is necessary.

Overall, the AMR-CESE-MHD method produces satisfactory simulations of the interaction between the solar wind and Saturn's magnetosphere. However, we need further improvements focusing on the following topics: (1) to take account of the plasma sources associated with Saturn itself, the rings, and the icy satellites into the source terms of the MHD equations, (2) to take the coupling of the magnetosphere and the ionosphere into consideration, (3) to study the dynamic responses of Saturn's magnetosphere to various solar wind conditions from observation data upstream of Saturn, and (4) to modify the newly established model to accommodate the studies of planets with strong intrinsic magnetic field (e.g., Jupiter) and planets with very weak or without intrinsic magnetic field (e.g., Mars and Venus).

Acknowledgments

The work was jointly supported by the National Basic Research Program of China (grants 2012CB825601, 2014CB845903, and 2012CB825604), the Knowledge Innovation Program of the Chinese Academy of Sciences (grant KZZD-EW-01-4), the National Natural Science Foundation of China (grants 41031066, 41231068, 41274192, 41074121, 41204127, 41174122, and 41474144), and the Specialized Research Fund for State Key Laboratories. The numerical calculation was completed on our SIGMA Cluster computing system at State Key Lab of Space weather/CAS. You may obtain the data by contacting Juan Wang at juanwang@spaceweather.ac.cn. We acknowledge the stimulating discussions with Xianzhe Jia from AOSS at University of Michigan.

Michael Balikhin thanks the reviewers for their assistance in evaluating the paper.

References

Alexeev, I. I., V. V. Kalegaev, E. S. Belenkaya, S. Y. Bobrovnikov, E. J. Bunce, S. W. H. Cowley, and J. D. Nichols (2006), A global magnetic model of Saturn's magnetosphere and a comparison with Cassini SOI data, *Geophys. Res. Lett.*, *33*, L08101, doi:10.1029/2006GL025896.

Dungey, J. (1961), Interplanetary magnetic field and the auroral zones, *Phys. Rev. Lett.*, *6*, 47–48.

Farris, M., and C. Russell (1994), Determining the standoff distance of the bow shock: Mach number dependence and use of models, *J. Geophys. Res.*, *99*, 17,681–17,689, doi:10.1029/94JA01020.

Feng, X. S., Y. Q. Hu, and F. S. Wei (2006), Modeling the resistive MHD by the CESE method, *Sol. Phys.*, *235*, 235–257, doi:10.1007/s11207-006-0040-6.

Feng, X. S., Y. F. Zhou, and S. T. Wu (2007), A novel numerical implementation for solar wind modeling by the modified conservation element/solution element method, *Astrophys. J.*, *655*, 1110–1126.

Feng, X. S., L. P. Yang, C. Q. Xiang, S. T. Wu, Y. F. Zhou, and D. K. Zhong (2010), Three-dimensional solar wind modeling from the Sun to Earth by a SIP-CESE MHD model with a six-component grid, *Astrophys. J.*, *723*, 300–319.

Feng, X. S., S. H. Zhang, C. Q. Xiang, L. P. Yang, C. Q. Jiang, and S. T. Wu (2011), A hybrid solar wind model of the CESE+HLL method with a Yin-Yang overset grid and an AMR grid, *Astrophys. J.*, *734*, 50–60.

Feng, X. S., L. P. Yang, C. Q. Xiang, C. W. Jiang, X. P. Ma, S. T. Wu, D. K. Zhong, and Y. F. Zhou (2012), Validation of the 3D AMR SIP–CESE solar wind model for four Carrington rotations, *Sol. Phys.*, *279*, 207–229, doi:10.1007/s11207-012-9969-9.

Feng, X. S., D. K. Zhong, C. Q. Xiang, and Y. Zhang (2013), GPU-accelerated computing of three-dimensional solar wind background, *Sci. Chin.*, *56*, 1864–1880, doi:10.1007/s11430-013-4661-y.

Fukazawa, K., S. Ogi, T. Ogino, and R. J. Walker (2007a), Magnetospheric convection at Saturn as a function of IMF B_Z, *Geophys. Res. Lett.*, *34*, L01105, doi:10.1029/2006GL028373.

Fukazawa, K., T. Ogino, and R. J. Walker (2007b), Vortex-associated reconnection for northward IMF in the Kronian magnetosphere, *Geophys. Res. Lett.*, *34*, L23201, doi:10.1029/2007GL031784.

Fukazawa, K., T. Ogino, and R. J. Walker (2012), A magnetohydrodynamic simulation study of Kronian field-aligned currents and auroras, *J. Geophys. Res.*, *117*, A02214, doi:10.1029/2011JA016945.

Hansen, K. C., T. I. Gombosi, D. L. DeZeeuw, C. P. T. Groth, and K. G. Powell (2000), A 3D global MHD simulation of Saturn's magnetosphere, *Adv. Space Res.*, *26*, 1681–1690, doi:10.1016/S0273-1177(00)00078-8.

Hansen, K. C., A. J. Ridley, G. B. Hospodarsky, N. Achilleos, M. K. Dougherty, T. I. Gombosi, and G. Tóth (2005), Global MHD simulations of Saturn's magnetosphere at the time of Cassini approach, *Geophys. Res. Lett.*, *32*, L20S06, doi:10.1029/2005GL022835.

Hill, T. W., et al. (2008), Plasmoids in Saturn's magnetotail, *J. Geophys. Res.*, *113*, A01214, doi:10.1029/2007JA012626.

Jackman, C. M., L. Lamy, M. P. Freeman, P. Zarka, B. Cecconi, W. Kurth, S. Cowley, and M. Dougherty (2009), On the character and distribution of lower-frequency radio emissions at Saturn and their relationship to substorm-like events, *J. Geophys. Res.*, *114*, A08211, doi:10.1029/2008JA013997.

Jackman, C. M., J. Slavin, and S. Cowley (2011), Cassini observations of plasmoid structure and dynamics: Implications for the role of magnetic reconnection in magnetospheric circulation at Saturn, *J. Geophys. Res.*, *116*, A10212, doi:10.1029/2011JA016682.

Jackman, C. M., N. Achilleos, S. W. Cowley, E. J. Bunce, A. Radioti, D. Grodent, S. V. Badman, M. K. Dougherty, and W. Pryor (2013), Auroral counterpart of magnetic field dipolarizations in Saturn's tail, *Planet. Space Sci.*, *82*, 34–42, doi:10.1016/j.pss.2013.03.010.

Jia, X., K. C. Hansen, T. I. Gombosi, M. G. Kivelson, G. Tóth, D. L. DeZeeuw, and A. J. Ridley (2012), Magnetospheric configuration and dynamics of Saturn's magnetosphere: A global MHD simulation, *J. Geophys. Res.*, *117*, A05225, doi:10.1029/2012JA017575.

Jiang, C. W., X. S. Feng, J. Zhang, and D. K. Zhong (2010), AMR simulations of magnetohydrodynamic problems by the CESE method in curvilinear coordinates, *Sol. Phys.*, *267*, 463–491.

Kanani, S., et al. (2010), A new form of Saturn's magnetopause using a dynamic pressure balance model, based on in situ, multi-instrument Cassini measurements, *J. Geophys. Res.*, *115*, A06207, doi:10.1029/2009JA014262.

Mitchell, D., et al. (2005), Energetic ion acceleration in Saturn's magnetotail: Substorms at Saturn?, *Geophys. Res. Lett.*, *32*, L20S01, doi:10.1029/2005GL022647.

Ogi, S., K. Fukazawa, and T. Ogino (2005), MHD simulation of the Saturnian magnetosphere, *Proc. ISSS*, *7*, 26–31.

Palmroth, M., P. Janhunen, T. I. Pulkkinen, and W. K. Peterson (2001), Cusp and magnetopause locations in global MHD simulation, *J. Geophys. Res.*, *106*, 29,435–29,450.

Powell, K. G., P. L. Roe, T. J. Linde, T. I. Gombosi, and D. L. DeZeeuw (1999), A solution-adaptive upwind scheme for ideal magnetohydrodynamics, *J. Comput. Phys.*, *154*, 284–309.

Russell, C., C. Jackman, H. Wei, C. Bertucci, and M. Dougherty (2008), Titan's influence on Saturnian substorm occurrence, *Geophys. Res. Lett.*, *35*, L12105, doi:10.1029/2008GL034080.

Samsonov, A. A., D. G. Sibeck, and J. Imber (2007), MHD simulation for the interaction of an interplanetary shock with the Earth's magnetosphere, *J. Geophys. Res.*, *112*, A12220, doi:10.1029/2007JA012627.

Tanaka, T. (1994), Finite volume TVD scheme on an unstructured grid system for three-dimensional MHD simulations of inhomogeneous systems including strong background potential field, *J. Comput. Phys.*, *111*, 381–389.

Thomsen, M. (2013), Saturn's magnetospheric dynamics, *Geophys. Res. Lett.*, *40*, 5337–5344, doi:10.1002/2013GL057967.

Vasyliūnas, V. (1983), *Plasma Distribution and Flow*, pp. 395–453, Cambridge Univ. Press, New York.

Walker, R. J., K. Fukazawa, T. Ogino, and D. Morozoff (2011), A simulation study of Kelvin-Helmholtz waves at Saturn's magnetopause, *J. Geophys. Res.*, *116*, A03203, doi:10.1029/2010JA015905.

Zhou, Y. F., and X. S. Feng (2013), MHD numerical study of the latitudinal deflection of coronal mass ejection, *J. Geophys. Res. Space Physics*, *118*, 6007–6018, doi:10.1002/2013JA018976.

Zieger, B., K. C. Hansen, T. I. Gombosi, and D. L. DeZeeuw (2010), Periodic plasma escape from the mass-loaded Kronian magnetosphere, *J. Geophys. Res.*, *115*, A08208, doi:10.1029/2009JA014951.